The Cryosphere

The modelled surface mass balance of the Antarctic Peninsula at 5.5 km horizontal resolution

J. M. van Wessem[1], **S. R. M. Ligtenberg**[1], **C. H. Reijmer**[1], **W. J. van de Berg**[1], **M. R. van den Broeke**[1], **N. E. Barrand**[2], **E. R. Thomas**[3], **J. Turner**[3], **J. Wuite**[4], **T. A. Scambos**[5], and **E. van Meijgaard**[6]

[1]Institute for Marine and Atmospheric Research Utrecht, Utrecht University, Utrecht, the Netherlands
[2]School of Geography, Earth and Environmental Sciences, University of Birmingham, Birmingham, UK
[3]British Antarctic Survey, Cambridge, UK
[4]ENVEO IT GmbH, Innsbruck, Austria
[5]National Snow and Ice Data Center, University of Colorado, Boulder, CO, USA
[6]Royal Netherlands Meteorological Institute, De Bilt, the Netherlands

Correspondence to: J. M. van Wessem (j.m.vanwessem@uu.nl)

Abstract. This study presents a high-resolution (~ 5.5 km) estimate of surface mass balance (SMB) over the period 1979–2014 for the Antarctic Peninsula (AP), generated by the regional atmospheric climate model RACMO2.3 and a firn densification model (FDM). RACMO2.3 is used to force the FDM, which calculates processes in the snowpack, such as meltwater percolation, refreezing and runoff. We evaluate model output with 132 in situ SMB observations and discharge rates from six glacier drainage basins, and find that the model realistically simulates the strong spatial variability in precipitation, but that significant biases remain as a result of the highly complex topography of the AP. It is also clear that the observations significantly underrepresent the high-accumulation regimes, complicating a full model evaluation.

The SMB map reveals large accumulation gradients, with precipitation values above 3000 mm we yr^{-1} in the western AP (WAP) and below 500 mm we yr^{-1} in the eastern AP (EAP), not resolved by coarser data sets such as ERA-Interim. The average AP ice-sheet-integrated SMB, including ice shelves (an area of 4.1×10^5 km^2), is estimated at 351 Gt yr^{-1} with an interannual variability of 58 Gt yr^{-1}, which is dominated by precipitation (PR) (365 ± 57 Gt yr^{-1}). The WAP (2.4×10^5 km^2) SMB (276 ± 47 Gt yr^{-1}), where PR is large (276 ± 47 Gt yr^{-1}), dominates over the EAP (1.7×10^5 km^2) SMB (75 ± 11 Gt yr^{-1}) and PR (84 ± 11 Gt yr^{-1}). Total sublimation is 11 ± 2 Gt yr^{-1} and meltwater runoff into the ocean is 4 ± 4 Gt yr^{-1}. There are no significant trends in any of the modelled AP SMB components, except for snowmelt that shows a significant decrease over the last 36 years (-0.36 Gt yr^{-2}).

1 Introduction

The Antarctic Peninsula (AP) is one of the most rapidly changing regions on Earth (Turner et al., 2005). Over the last 50 years, the AP has experienced a warming of up to 3 K which is among the highest on Earth (Bromwich et al., 2012), and has increasingly contributed to global sea level rise (Shepherd et al., 2012; Wouters et al., 2015). In addition, the AP is the only region of Antarctica that is warm enough for widespread surface melt to occur, which has increased unprecedentedly over the past 1000 years (Abram et al., 2013). Likely as a result of the increased melt rates, many of the ice shelves that fringe the AP have (partly) disintegrated in recent years (Cook et al., 2005), potentially following hydrofracturing of surface crevasses (Vaughan et al., 2003; Van den Broeke, 2005). In combination with warmer ocean currents melting the ice shelves from below (Pritchard et al., 2012; Wouters et al., 2015), the ice shelves lose their buttressing effect (Dupont and Alley, 2005), accelerating the AP glaciers flowing into the ice shelves, and raising sea level (Rignot et al., 2011; Shepherd et al., 2012; Scambos et al.,

2000). Increased snowfall in a warming climate (Davis et al., 2005) is only partly expected to compensate for increasing dynamical mass loss in the future (Barrand et al., 2013a). In order to quantify the mass changes of the AP and the associated sea level rise, an accurate estimate of the AP contemporary surface mass balance is essential.

The surface mass balance (SMB in $\mathrm{mm\,we\,yr^{-1}}$) is defined as the sum of all mass gains and losses of the ice sheet surface:

$$\mathrm{SMB} = \int_{\mathrm{year}} (\mathrm{PR} - \mathrm{SU_s} - \mathrm{SU_{ds}} - \mathrm{ER_{ds}} - \mathrm{RU})\mathrm{d}t, \qquad (1)$$

where PR represents total precipitation (snowfall plus rain), SU surface ($\mathrm{SU_s}$) plus drifting snow ($\mathrm{SU_{ds}}$) sublimation, $\mathrm{ER_{ds}}$ drifting snow erosion/deposition (caused by divergence/convergence in the horizontal drifting snow flux) and RU meltwater runoff, the amount of liquid water (melt and rain) that is not retained or refrozen in the snowpack. The mean area averaged SMB of the AP is 6 times larger than that of the total Antarctic ice sheet (AIS) (Van Lipzig et al., 2004), and AP melt rates are also relatively large due to its northerly location (Barrand et al., 2013b). The high accumulation rates are a result of the AP acting as an efficient mountain barrier, forcing large amounts of orographic precipitation along its windward slopes.

Measuring AP SMB is a complicated task, as the high precipitation rates and the steep mountainous (and inaccessible) terrain leave large regions devoid of observational data; most observations are therefore located in relatively dry areas and/or over the flat ice shelves which are easily accessible (Favier et al., 2013). Ice and firn core observations have identified a doubling of accumulation over the WAP since 1850 (Thomas et al., 2008), an increase in AP SMB over the last 50 years (Peel, 1992), and a large spatial variability of the SMB (Turner et al., 2002). To solve the limited coverage of these observations, remote sensing techniques are pivotal. However, remote sensing techniques, such as radar backscatter to identify melt episodes (Barrand et al., 2013b) or satellite products like the Gravity Recovery and Climate Experiment (GRACE; Tapley et al., 2004), often don't resolve the small-scale features of the AP SMB. Other methods, such as using ice discharge estimates to calculate the mass balance of the ice sheet, or satellite altimetry to measure elevation changes, need detailed SMB fields (Rignot et al., 2011; Mouginot et al., 2012; Wuite et al., 2015), or require a correction for firn processes (Gunter et al., 2009), which is dependent on the SMB. Therefore, for a realistic mass balance estimate, continuous SMB fields are necessary.

Regional atmospheric climate models (RCMs) realistically simulate the climate and SMB of the larger glaciated regions, such as Greenland (Fettweis, 2007; Van Angelen et al., 2013) and Antarctica (Bromwich, 2004; Lenaerts et al., 2012b). Moreover, RCMs have, in combination with a firn densification model (FDM, Ligtenberg et al., 2011), been used to simulate the interaction of the snowpack with the atmosphere and a changing climate (Ligtenberg et al., 2014; Kuipers Munneke et al., 2015), providing detailed information about meltwater percolation, refreezing and the stability of ice shelves (Kuipers Munneke et al., 2014).

The SMB and climate of the AP have been simulated before, at a relatively high (14 km) resolution, but for a short timespan (6 years) (Van Lipzig et al., 2004). Higher resolution simulations have also been performed, but without a high-resolution snow-routine (Bromwich, 2004; King et al., 2015). Recently, the regional atmospheric climate model RACMO2.3 was used at a horizontal resolution of 5.5 km to simulate the SMB of Patagonia (Lenaerts et al., 2014). In this study we use the same model and resolution to simulate the SMB of the AP for 1979–2014, the period for which reliable forcing data are available, coupling it to a FDM to calculate processes in the firnpack and, eventually, runoff. We discuss the SMB and its components, with a particular focus on meltwater and precipitation. We present the model and the observations used in Sect. 2, and evaluate the modelled SMB with in situ observations and discharge estimates in Sect. 3. In Sect. 4, we discuss gridded climate maps of SMB and its components, and discuss spatial and temporal variability. Finally, we present a discussion of the results and conclusions in Sects. 5 and 6.

2 Data and methods

2.1 Regional Atmospheric Climate Model RACMO2.3

The Regional Atmospheric Climate Model RACMO2.3 combines the dynamics package of the High Resolution Limited Area Model (HIRLAM) (Undén et al., 2002) with the physics package of the European Centre for Medium-range Weather Forecasts (ECMWF) Integrated Forecast System (IFS) (ECMWF-IFS, 2008). RACMO2.3 has been adapted for use over the large ice sheets of Greenland and Antarctica: it includes a multi-layer snow model to calculate melt, percolation, refreezing and runoff of liquid water (Ettema et al., 2010); a prognostic scheme to calculate surface albedo based on snow grain size (Kuipers Munneke et al., 2011); and a routine that simulates the interaction of drifting snow with the surface and the lower atmosphere (Lenaerts et al., 2012a). ERA-Interim re-analysis data with 6-hourly resolution from January 1979 to December 2014 (Dee et al., 2011) are used to force the model at the lateral atmospheric boundaries as well as at the lower ocean boundaries by prescribing sea ice fraction and sea surface temperatures. The model domain interior (Fig. 1) is allowed to evolve freely and a model time step of 2 min is used.

RACMO2.3 is a hydrostatic model that we run at a horizontal resolution of ~ 5.5 km and 40 vertical levels. At this resolution we assume the assumption of hydrostatic balance to hold, an assumption that is justified to some extent by ear-
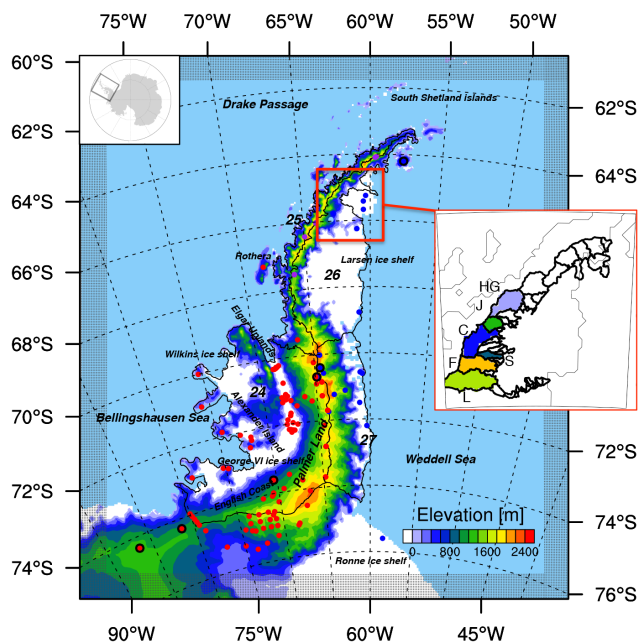
Figure 1. RACMO2.3 Antarctic Peninsula model domain (black box in inset map of Antarctica), boundary relaxation zone (dotted area, 16 grid points) and model surface topography (m). Locations of in situ SMB observations are marked (dots); ice cores, as used in Sect. 3.2, are highlighted (black circles). Colours of the dots indicate whether the observation lies in a WAP (red), EAP (blue) or spine (purple) height bin (see Sect. 3). Model topography is based on digital elevation models from Cook et al. (2012) for the region north of 70° S, and Bamber et al. (2009) south of 70° S. White areas represent floating ice shelves, colours represent the elevation of the grounded ice sheet. Zwally et al. (2012) drainage basins 24, 25, 26 and 27 are shown (black lines). One EAP in situ observation is shown in light blue for visibility. Inset denotes the six drainage basins of pre-acceleration Larsen B outlet glaciers: Starbuck (S), Flask (F), Leppard (L), Crane (C), Jorum (J) and Hektoria-Green (HG) from Wuite et al. (2015).

lier studies (Lenaerts et al., 2014; Van Wessem et al., 2015), although a non-hydrostatic model version will likely further improve the model output in terms of better resolved processes over sloping surfaces, such as foehn and katabatic winds that influence (drifting snow) sublimation and snowmelt fluxes (Cassano and Parish, 2000). The surface topography is based on a combination of the 100 m digital elevation model (DEM) from Cook et al. (2012) and the 1 km DEM from Bamber et al. (2009). The ice sheet mask is kept constant through the simulation, and includes the (former) Larsen B and Larsen A ice shelves. All integrated SMB estimates use basins number 24–27 from the basin definition from Zwally et al. (2012), and include Larsen B, but for calculations (e.g. yearly averages) after its disintegration (2003), Larsen B is excluded. For 1979–2014 averages, the full ice sheet mask including Larsen B is used. For further

details of the model the reader is referred to Van Wessem et al. (2015).

The model is initialized on 1 January 1979, with the atmospheric state and sea surface boundary conditions adopted from ERA-Interim reanalysis. The initial firnpack of the AP is inferred from a simulation with an offline firn densification model (FDM, Ligtenberg et al., 2011), which was driven by an earlier climatological simulation of the AP by RACMO2.3, largely comparable to the one used in this study. Runoff estimates are taken from the FDM, which was forced by RACMO2.3: the other SMB components are taken directly from RACMO2.3.

2.2 Firn densification model

The firn densification model (FDM) is a high-resolution version (~ 3000 layers in the vertical) of the internal snow model that is interactively coupled to RACMO2.3. It is a single column time-dependent model that describes the evolution of the firn layer. It calculates firn density, temperature and liquid water content evolution based on forcing at the surface by RACMO2.3 variables at 3-hourly resolution: surface temperature, accumulation and wind speed. Surface meltwater percolates into the model firn layer, where it can refreeze, be stored or percolate further down. The retention of meltwater is based on the "tipping-bucket" method (i.e. liquid water is stored in the first available layer and transported downwards only when it exceeds capillary forces). Liquid water that reaches the bottom of the firn layer and can neither refreeze nor be stored is removed as runoff (RU in Eq. 1). We do not use output from the internal snow model, because of small coding errors, but instead run the FDM offline, with the additional benefit of its higher vertical resolution. We found no significant differences due to, e.g. the interaction of the atmosphere with subsurface processes in the snow column. A detailed analysis of subsurface processes is beyond the scope of this study; here we focus on the integrated mass budget and the SMB. More details on the FDM can be found in Ligtenberg et al. (2011).

2.3 Observational data

2.3.1 In situ observations

We evaluate modelled SMB using 132 in situ observations, originating from various sources and methods, e.g. ice cores, stake arrays and bomb horizons (Fig. 1) (Turner et al., 2002; Favier et al., 2013; Scambos et al., 2014). Included in these data are five unpublished in situ observations from high elevations, obtained from a shallow ice core, sonic snow height measurements and camera observations of a snow stake over time (T. A. Scambos, personal communication, 2014). Also included are six ice core accumulation records: James Ross Island (Abram et al., 2011), Gomez (Thomas et al., 2008), two cores from Dyer Plateau, one to the east of the ice di-

vide (Thompson et al., 1994), one to the west of the ice divide (Arthern et al., 2010, E. R. Thomas, unpublished data), Bryan Coast and Ferrigno (E. R. Thomas, unpublished data). These records are additionally used to assess model interannual variability in Sect. 3.2.

We compare modelled SMB with in situ observations only for overlapping time periods, when available. When observations date from before 1979, or when the time of measurement is not known, they are compared with the climatological (1979–2014) modelled SMB. Only 38 SMB observations have an observation length > 5 years and these are used for model evaluation in Sect. 4. Note that for all comparisons, the observational data are compared with data from the nearest model grid point; no interpolation is performed.

2.3.2 Discharge estimates

We evaluate modelled SMB using 1995 pre-collapse discharge (D) estimates of six Larsen B outlet glaciers in the north-eastern AP. We assume these to be in balance (SMB − $D = 0$), as the data date from well before the significant thinning and retreat of the Larsen B ice shelf, that culminated in its disintegration in 2002 (Wuite et al., 2015); we exclude basins that are too small to be resolved by the model resolution, or were not in balance. This leaves six basins: Starbuck, Flask, Leppard, Crane, Jorum and Hektoria-Green, shown in Fig. 1. Assuming balance of these basins, a comparison with the climate average SMB for 1979–2014 is justified, and we directly compare discharge with RACMO2.3 SMB for this period.

3 Results: model evaluation

3.1 In situ observations

Figure 2 compares modelled (red) and observed (black) SMB for the locations of the in situ observations (averaged in elevation bins). As many SMB observations are clustered, i.e. mostly located on the ice shelves and locations of relatively low accumulation, we have binned the observations in 11 surface elevation bins, selected such that they span at least ∼ 75 m in elevation and contain at least 10 SMB data points. The bins are arranged from left to right in eight western AP (WAP) bins (W1–W8), one bin for the spine (S) and two bins for the eastern AP (EAP; E1–E2). For all other observations that are not located in any of the basins, but situated within the model domain, we define a 65° W longitude threshold: all observations west of this boundary represent the WAP, the others the EAP. Figure 2 shows that the model and the observations show relatively constant SMB values for the WAP and the EAP (< 1000 mm we yr^{-1}), and a pronounced peak in SMB over the spine. Variability between the different bins is caught well and simulated SMB is always within the standard deviation of the observations. For bins W2, W6 and W7 there is a slightly larger discrepancy with the observations.
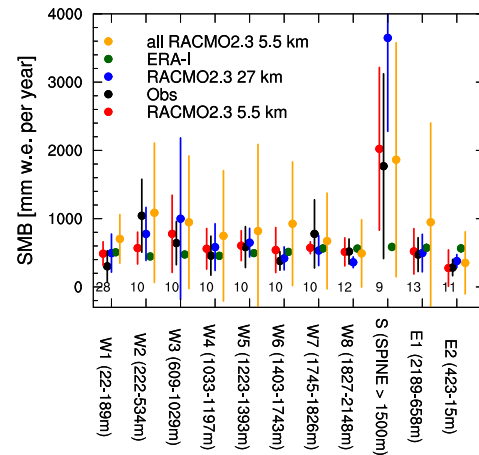

Figure 2. Modelled RACMO2.3 5.5 km (red), RACMO2.3 27 km (blue), ERA-Interim (green) and observed (black) SMB as a function of 11 elevation bins for all in situ SMB observations. The orange dots are the average SMB of all RACMO 5.5 km grid points in the elevation bins. The bins are arranged from west to east in three separate classes (WAP (W1–8), the spine (S) and the EAP (E1–2)), using the drainage basin definition from Zwally et al. (2012). Error bars represent 1 standard deviation within the bin and amount of observations in each bin is denoted within the plot. Further details are provided in the text (Sect. 2.3.1).

To explain this, we calculated the average of all model grid points within the respective bins (orange points). These averages are considerably higher than both the observed and modelled values, showing that the observations are biased towards regions of low accumulation.

Figure 3a presents the direct correlation between the model and the observations, both for the individual locations as for the 11 elevation bins. The SMB over the AP is highly variable and modelled SMB is poorly correlated with the individual observations ($r^2 = 0.25$, rc = 0.46), although the average bias is low (bias = 28.4 mm we yr^{-1}). The binned averages strongly improve the correlation ($r^2 = 0.8$) and the slope (rc = 0.97), demonstrating that larger-scale spatial variability is generally well captured. The EAP SMB is well simulated, especially the low SMB over the ice shelves, even though few EAP observations are available. For the WAP, the model overestimates SMB in relatively dry locations (George VI ice shelf and southern Palmer Land), while underestimating SMB in the wetter locations (coastal zones). This is likely related to an insufficient representation of orographic precipitation at 5.5 km. This could be a result of overly simple cloud physics (e.g. precipitation falls to the surface instantly, and is not transported across grid-boxes), and/or the model being hydrostatic, not effectively simulating vertical atmospheric motion, and/or the remaining underestimation of the surface slope (Van Wessem et al., 2015). The model does simulate the peak in SMB (∼ 2000 mm we yr^{-1}) of the northern spine bin (containing WAP and EAP observations > 1500 m eleva-
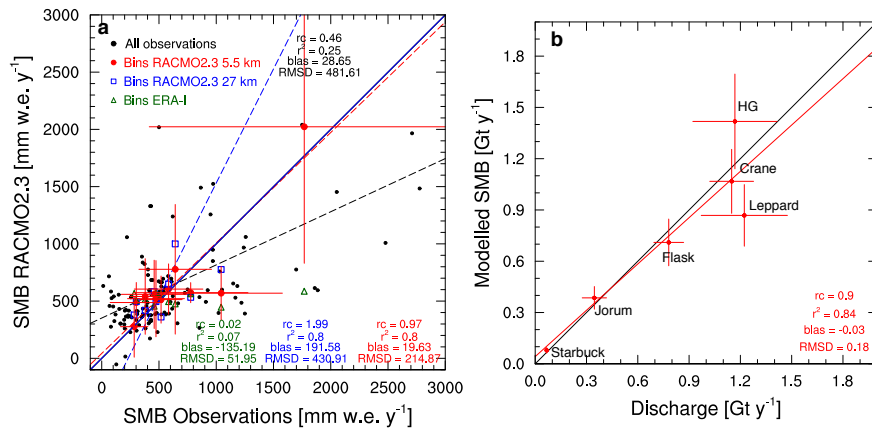
Figure 3. (a) Modelled RACMO2.3 SMB at 5.5 km as a function of in situ SMB observations (black dots), and the height bins as defined in Fig. 2 for RAMCO2.3 5.5 km (red dots), RACMO2.3 27 km (blue squares) and ERA-Interim (green triangles) in mm we yr^{-1}. Error bars represent 1 standard deviation within the height bins (for clarity error bars for RACMO2.3 27 km and ERA-Interim are not plotted). Dashed lines represent the linear regressions lines. Two locations with either observed or modelled SMB values > 3000 mm we yr^{-1}, as well as one binned 27 km location, are off the chart and are not shown for clarity. **(b)** Modelled RACMO2.3 SMB at 5.5 km (with 1 standard deviation) as a function of drainage basins discharge estimates (with uncertainty) (Wuite et al., 2015) in Gt yr^{-1}. The red line represents the regression line of modelled SMB with discharge estimates. Basin locations are shown in Fig. 1.

tion), despite the few observations and the very large spatial variability.

Figures 2 and 3a clearly present the main advantage of the high-resolution SMB product over low-resolution products such as RACMO2.3 at 27 km horizontal resolution (Van Wessem et al., 2014b), or the ERA-Interim re-analysis (Dee et al., 2011). At 27 km horizontal resolution the low accumulation regions are well represented, resulting in a similar correlation ($r^2 = 0.8$) as at 5.5 km. In two elevation bins the SMB is actually better represented than at 5.5 km, likely due to error compensation of positive and negative SMB biases. However, at 27 km the SMB at high elevations is poorly represented and the 5.5 km product shows a considerable improvement, especially over the spine. The advantage of the high-resolution product is more evident when compared to the re-analysis: even though the re-analysis captures the SMB at the middle elevation bins reasonably well, as a result of its coarse resolution (~ 80 km), it lacks the ability to resolve the steep SMB gradients, and the large SMB values at the higher elevations, as well as the low SMB over the WAP and EAP ice shelves. Another obvious difference is the small spatial variability in ERA-Interim, compared to RACMO2.3 and the observations.

3.2 Interannual variability

Figure 4 shows yearly modelled (red) and observed (black) SMB at the location of six ice cores. Modelled SMB to a large extent reproduces the observations. The model mainly underestimates the absolute SMB east and west of the ice divide at Dyer Plateau (Fig. 10c and d), where spatial variability is large, although for the western Dyer Plateau record the

modelled and observed variability matches relatively well, but both these records are very short. The records of Gomez, Bryan Coast and Ferrigno over the WAP, and James Ross Island over the EAP, match particularly well; the magnitude is simulated well by the model at these locations, and correlation coefficients are larger as well, although the model has difficulties in timing the SMB maxima at the Gomez and James Ross ice cores, especially earlier in the record. For James Ross Island this is likely related to the ice core being located on a small island with large elevation differences, and due to the observational record being compared with data from the nearest model grid point.

3.3 Discharge

We assessed modelled climatological SMB by comparing it to solid ice discharge estimates from glacier basins, for a time period when these were in approximate balance (pre-1995, Wuite et al., 2015). Figure 3b shows that modelled SMB matches the discharge estimates, especially for the smaller basins (Jorum, Starbuck and Flask). For the larger basins the representation is still generally good (bias < 30 %), especially considering the relatively small size of these basins (Fig. 1), and the large spatial SMB variability along the northern AP mountain spine.
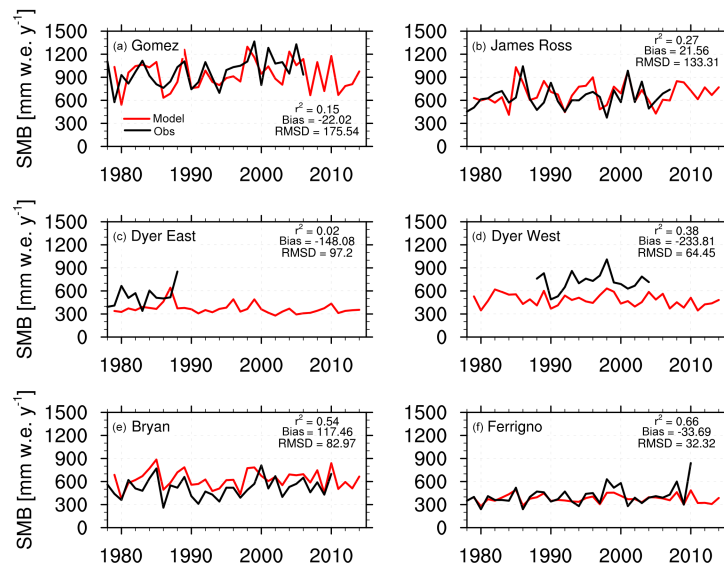
Figure 4. Modelled and observed yearly (1979–2014) SMB ($mm\,we\,yr^{-1}$) at locations of Gomez (**a**, 73° S, 70° W), James Ross Island (**b**, 64.12° S, 57.54° W), Dyer Plateau East (**c**, 70.4° S, 64.5° W), Dyer Plateau West (**d**, 70.7° S, 64.9° W), Bryan Coast (**e**, 74.3° S, 81.4° W) and Ferrigno (**f**, 74.3° S, 86.5° W) ice core sites. Statistics (r^2, bias and RMSD) are also given. Ice core locations are shown in Figs. 1 and 10.

4   Results: modelled SMB

4.1   Spatial variability

4.1.1   SMB components

Figure 5 presents average 1979–2014 AP SMB components (Eq. 1) and Fig. 6a the resulting SMB. Total precipitation ($PR = snowfall + rainfall$, Fig. 5a) dominates the AP SMB with values that are typically 1 order of magnitude larger than the other components, which is also the case for the whole AIS (Van Wessem et al., 2014a). PR shows large gradients (note the nonlinear scale in Figs. 5a and 6), with values ranging from $> 1000\,mm\,we\,yr^{-1}$ on the western slopes and the adjacent ocean, towards low values ($< 300\,mm\,we\,yr^{-1}$) on the eastern slopes and ice shelves. In particular the modelled precipitation rates in the north-western AP are extreme with rates of up to $5000\,mm\,we\,yr^{-1}$ on the lower windward slopes, equivalent to $\sim 15\,m$ of snowfall each year. This makes the AP among the wettest regions (in terms of snowfall) on Earth, comparable with the high snowfall rates ($3500\,mm\,we\,y^{-1}$) for Patagonia simulated with the same model (Lenaerts et al., 2014). These mountainous regions represent a steep barrier that is almost perpendicular to the strong circumpolar westerlies, causing very efficient orographically induced precipitation over the windward mountain slopes, and a strong precipitation shadow on the leeward slopes. These sharp gradients are widespread, especially in the WAP: for instance, precipitation rates towards the south are high as well, varying from $2500\,mm\,we\,yr^{-1}$ on the Elgar Uplands towards 1000–$2000\,mm\,we\,yr^{-1}$ on the west-

ern slopes of Palmer Land, with a distinct minimum over George VI ice shelf situated at the lee side of Alexander Island.

The second largest component is drifting snow sublimation (SU_{ds}, Fig. 5e), removing $\sim 50\,mm\,we\,yr^{-1}$ of snowfall, peaking in regions of high wind speed (Van Wessem et al., 2015). SU_{ds} is smaller at high elevations and the (western) mountain slopes, where winds are weaker; here a surface-based temperature inversion, and the associated increasing humidity with height, favours surface deposition ($SU_s \simeq -20\,mm\,we\,yr^{-1}$, Fig. 5d). Surface sublimation ($SU_s > 0$) mainly occurs over the flat ice shelves and the lower mountain slopes, typically removing $\sim 20\,mm\,we\,yr^{-1}$. The erosion of drifting snow (ER_{ds}) does not significantly contribute to the (integrated) SMB, but redistributes mass on a local scale with snow divergence/convergence rates up to $100\,mm\,we\,yr^{-1}$ on the AP slopes, closely following the topography. Snowmelt (M) is widespread below $2000\,m\,a.s.l.$, showing large spatial variability, with maxima up to $500\,mm\,we\,yr^{-1}$ over the north-eastern ice shelves, and with decreasing values towards higher elevations and/or latitudes. Most meltwater refreezes or is retained in the snowpack, and only a fraction runs off into the ocean. This happens mainly over Larsen B and northern Larsen C ice shelves, but also over Wilkins and northern George VI ice shelves, with runoff (RU) fluxes up to $300\,mm\,we\,yr^{-1}$. Over the lower slopes of the north-western mountain range, where both PR and M are large, the model also simulates small amounts of runoff ($\sim 50\,mm\,we\,yr^{-1}$).
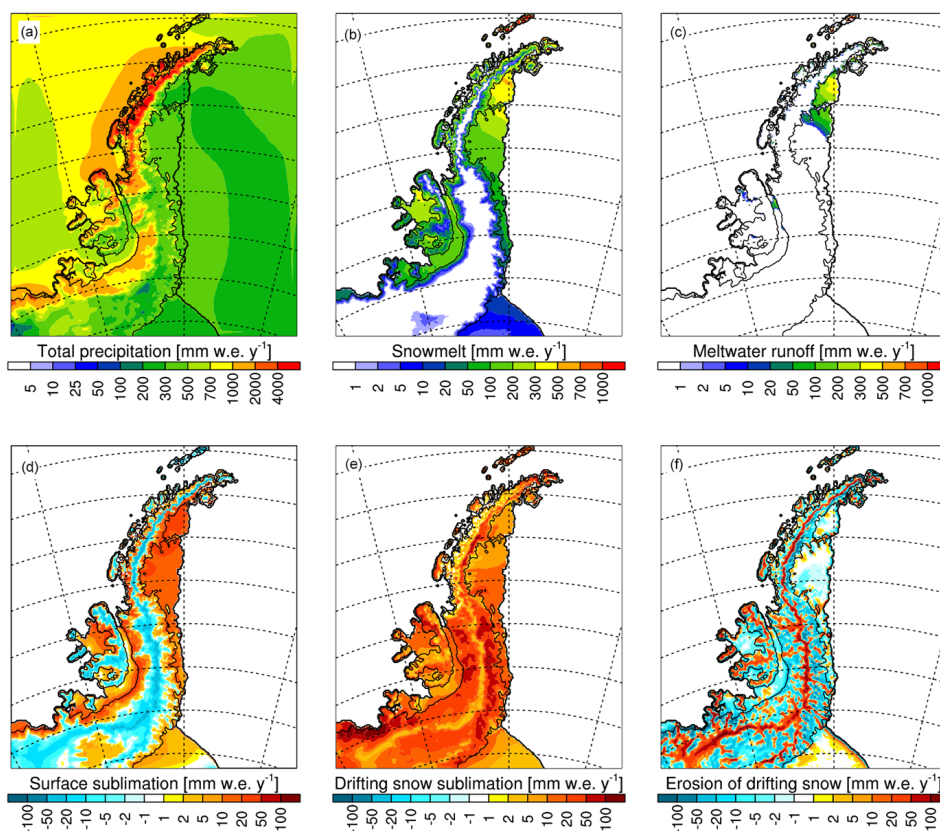
Figure 5. 1979–2014 average SMB components: total precipitation (snowfall + rain) **(a)**, snowmelt **(b)**, meltwater runoff **(c)**, total sublimation **(d)**, sublimation of drifting snow **(e)** and erosion of drifting snow **(f)** in mm we yr^{-1}. Note that ablation is defined positive in **(d–f)**. All fluxes are from RACMO2.3, except for runoff, which is calculated by the FDM that is forced by RACMO2.3 output.

4.1.2 SMB

Figure 6 presents the average modelled (1979–2014) SMB at 5.5 km (panel a) and 27 km (panel b) horizontal resolution, together with the in situ SMB observations with time spans > 5 years. SMB is largely similar to PR (Fig. 5a), with large west-to-east gradients, and peak SMB values around the WAP coastal regions, with large spatial variability that is controlled by the orography. Although a limited number of multi-year in situ observations are available, the modelled SMB patterns generally match with the observations: the large SMB values found only in a few observations are simulated well by the model, as well as the lower SMB values on the George VI and Larsen ice shelves. Over the former Larsen B ice shelf there is a mismatch: here, simulated RU reaches its maximum, and modelled SMB is negative (up to −100 mm we yr^{-1}). This negative SMB is not found in the pre-break-up observations, which show small but positive values. However, the model does agree that the minimum in SMB lies in this area. Furthermore, for unknown reasons, the SMB is considerably overestimated at two locations, on Adelaide Island, and slightly eastwards, a region of large variability (Turner et al., 2002).

At 27 km horizontal resolution (Fig. 6) the spatial pattern in SMB is largely similar to that at 5.5 km (also see Fig. 3). The main advantage of the high-resolution product is that it better resolves the SMB gradients, the peak SMB, as well as the small islands and narrow ice-shelves.

4.2 Average integrated SMB

Table 1 summarises the integrated WAP (basins 24/25 from Zwally et al., 2012), EAP (basins 26/27) and total (all basins) SMB values. The total AP SMB amounts to 351 Gt yr^{-1}, which is ∼ 20 % of the total integrated SMB for the AIS as found in Van Wessem et al. (2014b), even though its area (4.1×10^5 km^2) is only 3 % of the total AIS. The SMB over the WAP (276 Gt yr^{-1}) is considerably larger than that of the EAP (75 Gt yr^{-1}), although the larger area of the WAP (2.4×10^5 km^2) compared to that of the EAP (1.7×10^5 km^2) partly accounts for the difference. The large west-to-east differences are due to PR, that is 365 Gt yr^{-1} in total, 281 Gt yr^{-1} over the WAP and 84 Gt yr^{-1} over the EAP. Of PR, 99 % is snowfall (363 Gt yr^{-1}); rainfall is small (3 Gt yr^{-1}). Total sublimation is 11 Gt yr^{-1}, dominated by SU$_{ds}$ (9 Gt yr^{-1}). In contrast to the AIS, snowmelt over the AP is widespread, similar in extent to microwave satellite ob-
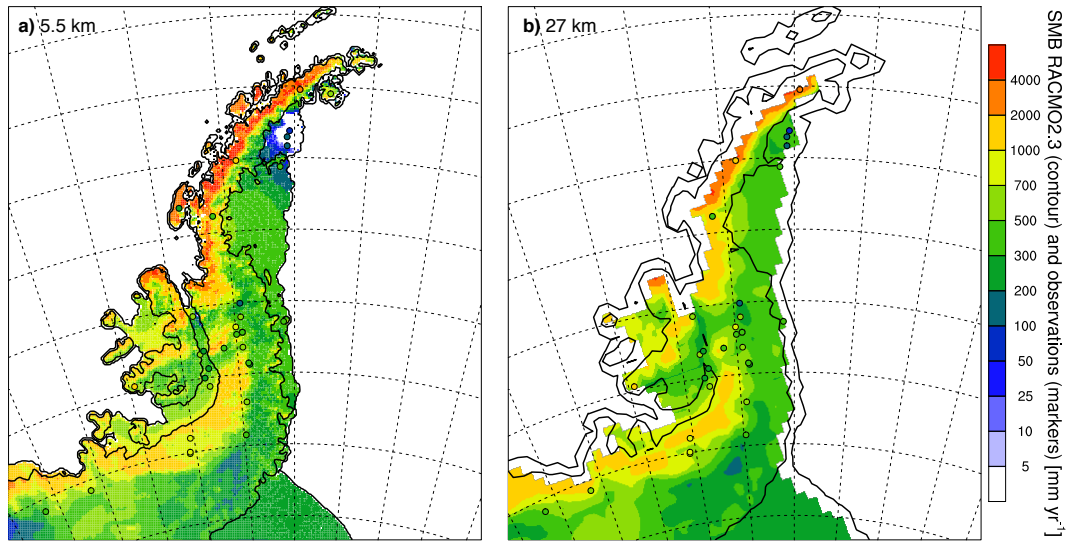
Figure 6. Modelled SMB (colours) and observations (markers) in mm we yr^{-1} at 5.5 km (**a**) and 27 km (**b**) horizontal resolution (Van Wessem et al., 2014b). Observations are from Turner et al. (2002), Favier et al. (2013) and Scambos et al. (2014) and sources noted in Sect. 2.3, and only shown if they represent a period > 5 years. Modelled SMB is the 1979–2014 climatological average. At both resolutions only ice sheet grid points are shown.

Table 1. AP integrated values of mean SMB components [Gt yr^{-1}] with interannual variability σ: total (snow + rain) precipitation (PR), snow, rain, total sublimation (SU$_{tot}$), surface sublimation (SU$_s$), drifting snow sublimation (SU$_{ds}$), drifting snow erosion (ER$_{ds}$), runoff (RU), snowmelt (M) and refreezing (RF). All values are calculated for basins 24–27 of Zwally et al. (2012), over a total AP area of 4.1×10^5 km^2. For WAP and EAP values, basins 24/25 and 26/27 are used, respectively. Values are calculated from yearly averages; from 2003 onwards integrated values represent the ice shelf excluding Larsen B ice shelf.

	mean	σ	EAP	σ	WAP	σ
Area (km^2)	4.1×10^5	–	2.4×10^5	–	1.7×10^5	
SMB	351	58	75	11	276	47
PR	365	57	84	10	281	47
snow	363	56	85	10	279	46
rain	3	1	0.5	0	2.2	1
SU	11	2	5.6	1	5.1	1
SU$_{ds}$	9	2	4.1	1	5	1
SU$_s$	2	0	1.6	0	0.1	0
ER$_{ds}$	1	0	−0.6	0	1.4	0
M	34	15	18.7	9	15.5	6
RF	35	13	17.2	6	17.5	7
RU	4	4	3.8	4	0.2	0

Figure 7. Yearly average SMB (**a**) and SMB components (**b**) in Gt yr^{-1}. For SMB, values for the WAP (red) and the EAP (blue) are shown. SMB is integrated over basins 24, 25, 26 and 27 from Zwally et al. (2012). Trend lines are only shown if significant. From 2003 onwards integrated values represent the ice shelf excluding Larsen B ice shelf.

4.3 Temporal variability

4.3.1 Interannual variability

Figure 7 shows yearly average SMB values and the largest SMB components; for integrated values after 2003 we exclude Larsen B ice shelf. Total AP SMB (Fig. 7a) has an interannual variability of 58 Gt yr^{-1} (15 % of mean SMB, absolute values shown in Table 1) and shows no signifi-

servations (Barrand et al., 2013b), and three times larger than the rest of the AIS combined (34 vs. 11 Gt yr^{-1}, Van Wessem et al., 2014b). Most meltwater (and rainfall) refreezes in the snowpack (RF = 33 Gt yr^{-1}) but a small fraction runs off into the ocean (RU = 4 Gt yr^{-1}); most RU is present over the EAP, in particular over the Larsen B ice shelf (3 Gt yr^{-1}).

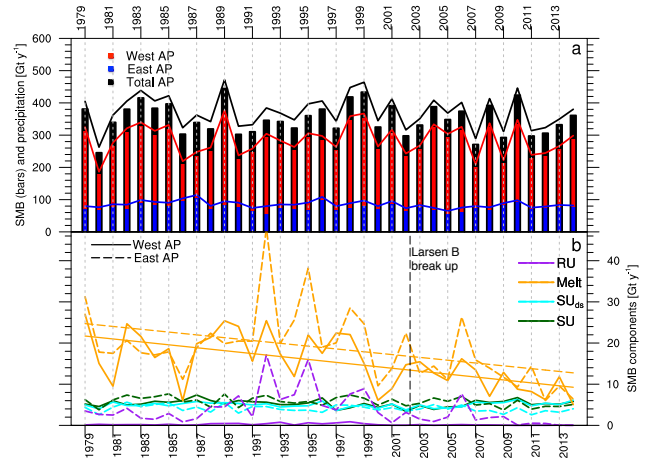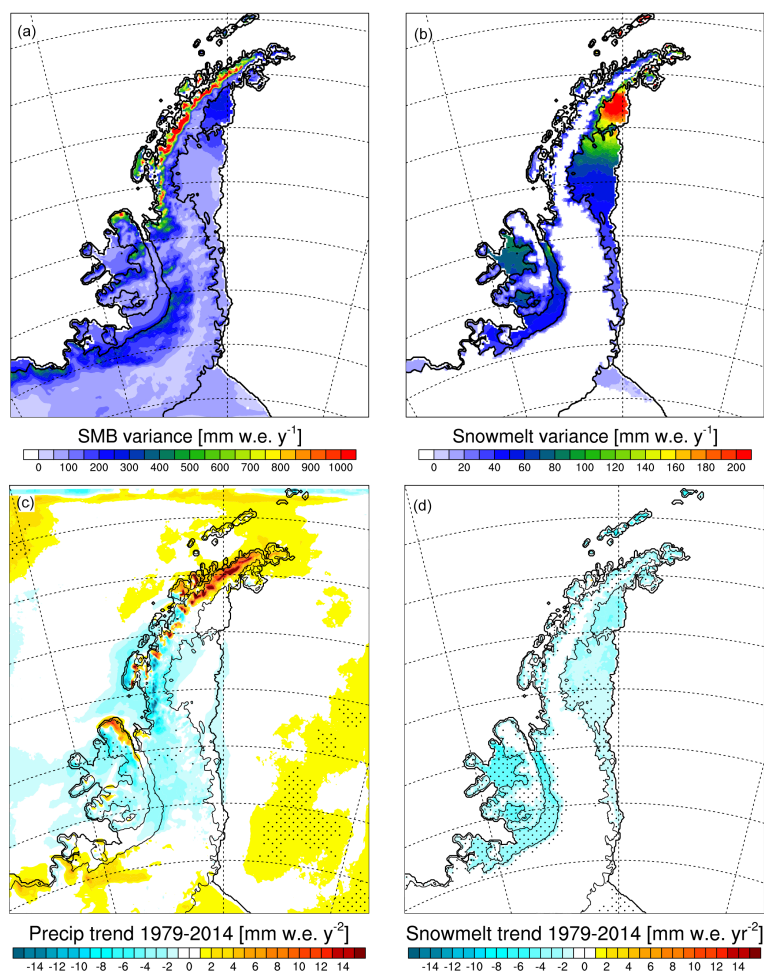**Figure 8.** Interannual variability (1 standard deviation, detrended) of SMB components for 1979–2014: SMB **(a)**, and snowmelt **(b)**, in mm we yr^{-1}. 1979–2014 trends of precipitation **(c)** and snowmelt **(d)** in mm we yr^{-2}. Stippled pattern represents trends that are significant > 95 %.

cant trend. Precipitation has a similar interannual variability of 57 Gt yr^{-1}. The most positive SMB year is 1989 with 445 Gt yr^{-1}, being significantly wetter than the driest year (1980, 246 Gt yr^{-1}), relatively a much larger difference than for the whole AIS (Lenaerts et al., 2012b), which is expected as over larger regions differences cancel out. Variability in sublimation and drifting snow sublimation is low, and comparable for the WAP and the EAP (1 Gt yr^{-1}). Of the SMB components (other than RU, that is small), the variability of M is the largest (15 Gt yr^{-1}, 45 % of the mean), reaching its peak in 1992 (73 Gt yr^{-1}), and minima (~ 11 Gt yr^{-1}) in 1986 and 2014. EAP melt rates are higher by 3 Gt yr^{-1} (relatively even higher as the area of the EAP is smaller than that of the WAP), but the timing of the maxima in M is similar. Simulated integrated AP snowmelt is lower than, but the variability and maxima are comparable to, the melt rates from Kuipers Munneke et al. (2012), (34 ± 15 and 57 ± 21 Gt yr^{-1}, respectively) that were calculated with RACMO2.1 at 27 km horizontal resolution. Even though the

model physics has been updated and RACMO2.3 generally simulates less melt over the AIS (Van Wessem et al., 2014b), differences between both studies are explained by the use of a more sophisticated snowpack initialization in this study, and a different integration domain; i.e. in Kuipers Munneke et al. (2012) Larsen B is included for the whole period and the domain extends further south.

For none of the variables a significant trend is simulated, except for snowmelt (significance level > 99 %). Snowmelt has decreased by the same amount (-0.35 Gt yr^{-2}) over the WAP and the EAP, which is likely related to the significant and widespread cooling over most of the AP in the last decade (Van Wessem et al., 2015). Runoff of meltwater is small but its variability is as high as its mean (4 Gt yr^{-1}); peak years, 1992 and 1995 in particular, reach values of up to 15 Gt yr^{-1}, following the peaks in snowmelt. In contrast to M, RU over the WAP and EAP shows large differences. Despite the higher temperatures, a thick firnpack exists over the WAP, as a result of the higher snowfall rates, permitting
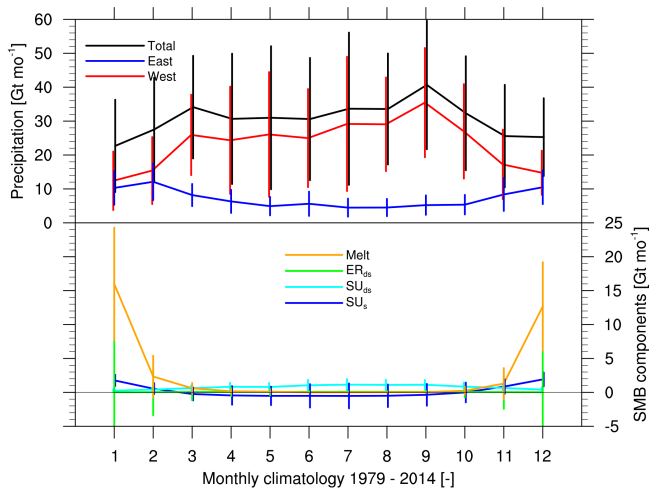
Figure 9. 1979–2014 monthly climatology of SMB components: top panel shows total precipitation (snowfall + rain) averaged for the WAP drainage basins (red line), the EAP (blue), and total (black). Bottom panel shows total (WAP + EAP) snowmelt (orange), erosion of drifting snow ER_{ds} (green), drifting snow sublimation SU_{ds} (cyan), and surface sublimation/deposition (blue). All variables in $Gt\,mo^{-1}$.

most meltwater to refreeze in the available pore space. Over the eastern ice shelves there is hardly any pore space present in the firn and a larger fraction of meltwater runs off, especially over Larsen B ice shelf before 2003.

Figure 8 shows maps of interannual variability in SMB and M. SMB variability (Fig. 8a) shows no unexpected patterns for most of the domain, mostly following the regions of high absolute SMB. Relatively, SMB variability peaks over George VI, Larsen B and the northern part of Larsen C ice shelves ($> 40\%$). This is clearly related to RU (not shown), which in turn is controlled by snowmelt variability (Fig. 8b), that peaks towards the northern parts of the ice shelves. It is clear that dry regions, which experience significant melt, show the largest interannual (relative) SMB variability. Interestingly, these coincide with the EAP ice shelves, which are also sensitive to disintegration. The other SMB components (not shown) have low variability and show no pronounced patterns.

There are no trends in integrated precipitation, but Fig. 8c shows that large significant trends exist locally, e.g. on Alexander Island and in the Weddell Sea. The model simulates large positive trends over the northerly slopes of the WAP ($15\,mm\,we\,yr^{-2}$), but these are not significant as these locations also experience large interannual variability. These trends are related to enhanced upper atmosphere northerly winds (Thomas et al., 2013; Van Wessem et al., 2015). Negative trends in snowmelt (Fig. 8d) are more significant on the WAP than on the EAP ice shelves, and show a uniform pattern.

4.3.2 Seasonal cycle

Figure 9 shows the average seasonal cycle (1979–2014) of SMB components. Integrated AP precipitation has a pronounced seasonality, with considerably larger values in winter than in summer. In winter, the stronger westerlies create more orographic precipitation over the WAP mountain slopes. In addition, WAP (and hence total) precipitation shows two peaks in March and in October, that are related to the semiannual oscillation (Van Loon, 1967; Van Den Broeke, 1998), in agreement with observational data from surface stations (Turner et al., 1997; Kirchgäßner, 2011). Over the EAP, the precipitation seasonality is reversed: here precipitation peaks in summer, reaching values almost as high as in the WAP summer, and decreases to a relatively constant minimum in winter 1 order of magnitude lower than over the WAP. Over the EAP, most summer precipitation originates from the Weddell Sea; when a minimum of sea-ice cover is reached in summer, moist ocean air is transported to the eastern ice shelves.

The other SMB components have lower magnitudes and show varying seasonal patterns. Snowmelt is absent in winter, and reaches its peak ($13\,Gt\,yr^{-1}$) in December and January. SU_s is negative in winter ($-1\,Gt\,yr^{-1}$), when a persistent surface-based temperature inversion favours surface deposition. This positive contribution to the SMB is compensated by the stronger wintertime winds removing mass by SU_{ds}. In summer, SU_{ds} drops off as winds are weaker and the snowpack gets warmer and denser. SU_s increases with surface temperature, and up to $3\,Gt\,yr^{-1}$ of snow is removed. Finally, ER_{ds} is very low year-round ($< 0.1\,Gt\,yr^{-1}$).

4.3.3 Spatial coherence of modelled precipitation

To illustrate the spatial coherence of AP SMB, Fig. 10 shows the spatial correlation of the modelled yearly time series at the six ice core locations of Sect. 3.2, with all other points in the model domain. Figure 10a shows that the SMB simulated at the location of the Gomez ice core, in south-western Palmer Land, is strongly and significantly ($> 99\%$) correlated over the whole WAP, supporting the strong spatial coherence that was also found for (observed) temperature in King (2003). Simultaneously there is a negative correlation over the north-eastern AP, and Larsen B and C ice shelves, showing that high WAP SMB rates are coinciding with dry conditions over this region, a coherence not found in King (2003). Figure 10b identifies the spatial coherence of this location as well: when SMB is large at James Ross Island, it is large over the northern EAP ice shelves and sea-ice, while over the WAP an insignificant correlation is found. Figure 10c shows that the SMB time series simulated at the Dyer Plateau ice core location, slightly east of the ice divide, is highly correlated with and representative of the adjacent EAP. Simultaneously, the second ice core at Dyer Plateau (Fig. 10d), located only 30 km westwards, and the Bryan
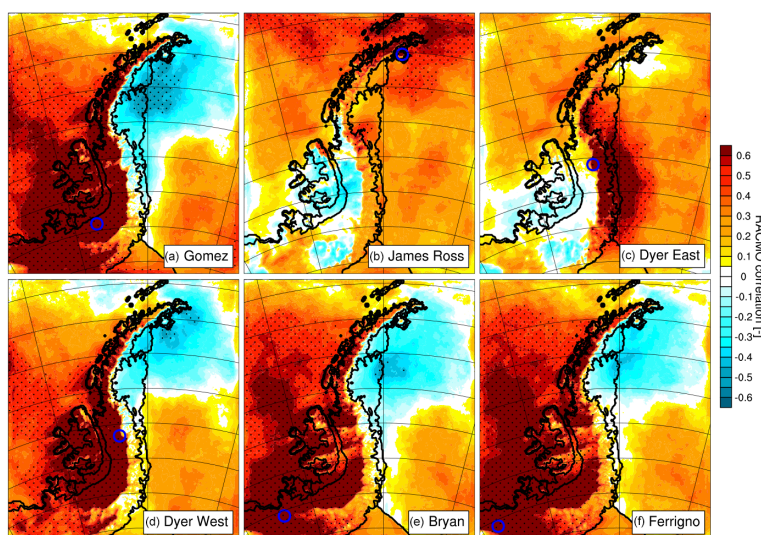
Figure 10. Correlation of modelled yearly (1979–2014) SMB at locations of Gomez (**a**, 73° S, 70° W), James Ross Island (**b**, 64.12° S, 57.54° W), Dyer Plateau East (**c**, 70.4° S, 64.5° W), Dyer Plateau West (**d**, 70.7° S, 64.9° W), Bryan Coast (**e**, 74.3° S, 81.4° W) and Ferrigno (**f**, 74.3° S, 86.5° W) ice cores, with all other points in the model domain. Stippled pattern represents significant correlations > 99 %. Locations of ice cores are denoted by blue circles. Note that over the sea-ice/ocean SMB = PR − SU.

Coast and Ferrigno ice cores (Fig. 10e and f), all located on the WAP, show completely opposite correlations, that closely resemble that of the Gomez ice core. These correlation maps clearly highlight the different forcing mechanisms of SMB on the WAP and EAP and the distinct and sharp climatic differences between both sides of the AP: over the WAP, snowfall is orographically induced, while over the EAP snowfall events are triggered by low pressure systems over the Weddell Sea.

5 Discussion

Although RACMO2.3 simulates the AP SMB with reasonable accuracy, the scarcity of observational data hampers a more thorough model assessment; more observational data should therefore be obtained, especially from higher elevations and areas with large snowfall rates. The comparison suggests that there are a number of potential problems. Not all local topographic detail (often at scales of < 1 km) is resolved at the 5.5 km model resolution. As a result the slope and the height of the orographic barrier of the AP are still underestimated, negatively affecting the simulated uplift of air and, consequently, precipitation and atmospheric foehn winds. In previous studies (Kuipers Munneke et al., 2012; Barrand et al., 2013b; Trusel et al., 2013), it was suggested that increasing the horizontal resolution from 27 km to the current value of 5.5 km would better resolve EAP surface melt, which is strongly related to the foehn winds. While the increase in resolution is clearly an improvement for other topography related variables, it appears that these foehn winds are not yet sufficiently resolved. However, further increas-

ing the resolution potentially moves the model beyond the limits of the hydrostatic assumption, and the use of a non-hydrostatic model would then become mandatory. Luckman et al. (2014) show that the non-hydrostatic, high-resolution (1.5 km) UTM model more efficiently resolves these foehn patterns. Cassano and Parish (2000) discussed the effects of a non-hydrostatic model on katabatic winds, which are also strongly related to the topography, and found that biases are relatively independent of the resolution.

Over the WAP there likely is a westward displacement of precipitation due to the model not taking into account horizontal advection of precipitation. In the current model version, precipitation is assumed to reach the surface instantly within the grid box where it is generated. Ideally precipitation, in particular snow which has a relatively low fall speed, must be modelled as a prognostic variable in order to capture its fall time and horizontal displacement. Van Lipzig et al. (2004) estimated that, with mean wind speeds of $\sim 7 \, \mathrm{m \, s^{-1}}$ for this region, snowfall could be advected over a distance of $\sim 10 \, \mathrm{km}$, i.e roughly two grid boxes at 5.5 km resolution simulation.

Currently, the only prognostic cloud variables are cloud fraction and cloud condensate that, together with temperature, determine the fractionation of cloud ice and cloud liquid water. An explicit treatment of liquid and solid cloud content is more physical than the current implicit treatment using temperature. Improving this necessitates the inclusion of prognostic precipitation in future simulations, which potentially leads to more (and thicker) clouds to be advected over the mountain range, as well as an improvement of the biases

in the downwelling radiative fluxes as found by King et al. (2015).

6 Summary and conclusions

We used the regional atmospheric climate model RACMO2.3 and a firn densification model (FDM) to simulate the SMB of the Antarctic Peninsula at a horizontal resolution of 5.5 km. RACMO2.3 is forced by ERA-Interim reanalysis at the lateral boundaries, and the snowpack is initialized with output from the FDM. We have evaluated the simulated SMB by comparison with 132 in situ SMB observations and six glacier discharge basins, both showing reasonable agreement. Most model biases are likely due to the still limited horizontal resolution, and limitations in the model formulation, e.g. the model being hydrostatic and precipitation not being treated as a prognostic variable which can be advected. However, the observations show a large over-representation from areas of low accumulation, especially over the western AP (WAP), and more observations are needed at higher elevations, regions of high accumulation and from the eastern AP (EAP), for a more robust model evaluation.

Integrated over four AP drainage basins (Zwally et al., 2012), the SMB amounts to $351 \pm 58 \, \mathrm{Gt \, yr^{-1}}$ ($\sigma = $ interannual variability), more or less equal to total precipitation ($365 \pm 57 \, \mathrm{Gt \, yr^{-1}}$), indicating that this is by far the dominant SMB component. The other components are more than 1 order of magnitude smaller, with drifting snow sublimation being the largest ($9 \pm 1.5 \, \mathrm{Gt \, yr^{-1}}$). Runoff is small ($4 \pm 4 \, \mathrm{Gt \, yr^{-1}}$) as most meltwater ($34 \pm 15 \, \mathrm{Gt \, yr^{-1}}$) and rainfall refreezes ($33 \pm 12 \, \mathrm{Gt \, yr^{-1}}$) in the cold firn, but is locally important on Larsen B, Larsen C and George VI ice shelves, and over the north-western AP with values up to $200 \, \mathrm{mm \, we \, yr^{-1}}$.

Pronounced differences in SMB exist between the WAP and EAP, and the AP spine acts as a sharp climate barrier. The SMB over the WAP amounts to $276 \pm 47 \, \mathrm{Gt \, yr^{-1}}$, nearly a factor of 4 larger than that over the EAP ($75 \pm 11 \, \mathrm{Gt \, yr^{-1}}$), resulting from the extreme orographic precipitation ($> 3000 \, \mathrm{mm \, we \, yr^{-1}}$) the model simulates over the windward mountain slopes, especially in winter. Over the EAP, the seasonality in SMB is reversed, peaking in summer when sea-ice extent in the Weddell Sea is smallest and synoptic weather systems transport clouds to the AP from the east. The other SMB components do not show these large west-to-east differences, with the exception of runoff. While melt rates are relatively similar over both the WAP and the EAP (18.7 ± 9, $15.5 \pm 6 \, \mathrm{Gt \, yr^{-1}}$), on the WAP most meltwater is retained or refreezes in the snowpack, that contains a large amount of pore space as a result of the large WAP snowfall rates. On the EAP, snowmelt often exceeds precipitation, and insufficient pore space is available for the meltwater to refreeze in, resulting in meltwater runoff in the ocean ($4 \pm 4 \, \mathrm{Gt \, yr^{-1}}$). This makes total sublimation the largest ablation term in the integrated AP surface mass budget ($11 \pm 2 \, \mathrm{Gt \, yr^{-1}}$), which is primarily determined by drifting snow sublimation ($9 \pm 1 \, \mathrm{Gt \, yr^{-1}}$).

This new high-resolution AP data set considerably adds to the current lower resolution data sets such as ERA-Interim, or lower resolution simulations with RACMO2.3, as the mountainous terrain is much better resolved. These data can be used, in combination with satellite products such as GRACE and radar/laser altimetry, to better understand the changes of AP glaciers and ice shelves.

In order to further improve model results, a computationally more expensive non-hydrostatic model might be used for longer climate-scale simulations of specifically selected small and topographically complex areas of the AP. Moreover, the FDM can be updated to better represent meltwater percolation and refreezing, e.g. taking into account non-homogenous meltwater percolation. Additionally, more observational data of the AP, both remote sensing and in situ data, should be acquired for improved model evaluation.

Edited by: M. Tedesco

References

Abram, N. J., Mulvaney, R., and Arrowsmith, C.: Environmental signals in a highly resolved ice core from James Ross Island, Antarctica, J. Geophys. Res., 116, 1–15, doi:10.1029/2011JD016147, 2011.

Abram, N. J., Mulvaney, R., Wolff, E. W., Triest, J., Kipfstuhl, S., Trusel, L. D., Vimeux, F., Fleet, L., and Arrowsmith, C.: Acceleration of snow melt in an Antarctic Peninsula ice core during the twentieth century, Nat. Geosci., 6, 404–411, doi:10.1038/ngeo1787, 2013.

Arthern, R. J., Vaughan, D. G., Rankin, A. M., Mulvaney, R., and Thomas, E. R.: In situ measurements of Antarctic snow compaction compared with predictions of models, J. Geophys. Res., 115, F03011, doi:10.1029/2009JF001306, 2010.

Bamber, J. L., Gomez-Dans, J. L., and Griggs, J. A.: A new 1 km digital elevation model of the Antarctic derived from combined satellite radar and laser data – Part 1: Data and methods, The Cryosphere, 3, 101–111, doi:10.5194/tc-3-101-2009, 2009.

Barrand, N. E., Hindmarsh, R. C. A., Arthern, R. J., Williams, C. R., Mouginot, J., Scheuchl, B., Rignot, E., Ligtenberg, S. R. M., Van Den Broeke, M. R., Edwards, T. L., Cook, A. J., and Simonsen, S. B.: Computing the volume response of the Antarctic Peninsula ice sheet to warming scenarios to 2200, J. Glaciol., 59, 397–409, doi:10.3189/2013JoG12J139, 2013a.

Barrand, N. E., Vaughan, D. G., Steiner, N., Tedesco, M., Kuipers Munneke, P., van den Broeke, M. R., and Hosking, J. S.: Trends in Antarctic Peninsula surface melting conditions from observations and regional climate modeling, J. Geophys. Res.-Earth, 118, 315–330, doi:10.1029/2012JF002559, 2013b.

Bromwich, D. H.: Modeled Antarctic Precipitation. Part I: Spatial and Temporal Variability, J. Climate, 17, 427–448, 2004.

Bromwich, D. H., Nicolas, J. P., Monaghan, A. J., Lazzara, M. A., Keller, L. M., Weidner, G. A., and Wilson, A. B.: Central West Antarctica among the most rapidly warming regions on Earth, Nat. Geosc., 6, 139–145, doi:10.1038/ngeo1671, 2012.

Cassano, J. J. and Parish, T. R.: An Analysis of the Nonhydrostatic Dynamics in Numerically Simulated Antarctic Katabatic Flows*, J. Atmos. Sci., 57, 891–898, doi:10.1175/1520-0469(2000)057<0891:AAOTND>2.0.CO;2, 2000.

Cook, A. J., Fox, A. J., Vaughan, D. G., and Ferrigno, J. G.: Retreating glacier fronts on the Antarctic Peninsula over the past half-century, Science, 308, 541–544, doi:10.1126/science.1104235, 2005.

Cook, A. J., Murray, T., Luckman, A., Vaughan, D. G., and Barrand, N. E.: A new 100-m Digital Elevation Model of the Antarctic Peninsula derived from ASTER Global DEM: methods and accuracy assessment, Earth Syst. Sci. Data, 4, 129–142, doi:10.5194/essd-4-129-2012, 2012.

Davis, C. H., Li, Y., McConnell, J. R., Frey, M. M., and Hanna, E.: Snowfall-driven growth in East Antarctic ice sheet mitigates recent sea-level rise, Science, 308, 1898–1901, doi:10.1126/science.1110662, 2005.

Dee, D. P., Uppala, S. M., Simmons, A. J., Berrisford, P., Poli, P., Kobayashi, S., Andrae, U., Balmaseda, M. A., Balsamo, G., Bauer, P., Bechtold, P., Beljaars, A. C. M., Van de Berg, L., Bidlot, J., Bormann, N., Delsol, C., Dragani, R., Fuentes, M., Geer, A. J., Haimberger, L., Healy, S. B., Hersbach, H., Hólm, E. V., Isaksen, L., Kållberg, P., Köhler, M., Matricardi, M., McNally, A. P., Monge-Sanz, B. M., Morcrette, J. J., Park, B. K., Peubey, C., de Rosnay, P., Tavolato, C., Thépaut, J. N., and Vitart, F.: The ERA-Interim reanalysis: configuration and performance of the data assimilation system, Q. J. Roy. Meteor. Soc., 137, 553–597, doi:10.1002/qj.828, 2011.

Dupont, T. K. and Alley, R. B.: Assessment of the importance of ice-shelf buttressing to ice-sheet flow, Geophys. Res. Lett., 32, 1–4, doi:10.1029/2004GL022024, 2005.

ECMWF-IFS: Part IV : Physical Processes (CY33R1), Tech. Rep. June, available at: http://www.ecmwf.int/research/ifsdocs/CY33r1/PHYSICS/IFSPart4.pdf (last access: October 2012), 2008.

Ettema, J., van den Broeke, M. R., van Meijgaard, E., van de Berg, W. J., Box, J. E., and Steffen, K.: Climate of the Greenland ice sheet using a high-resolution climate model – Part 1: Evaluation, The Cryosphere, 4, 511–527, doi:10.5194/tc-4-511-2010, 2010.

Favier, V., Agosta, C., Parouty, S., Durand, G., Delaygue, G., Gallée, H., Drouet, A.-S., Trouvilliez, A., and Krinner, G.: An updated and quality controlled surface mass balance dataset for Antarctica, The Cryosphere, 7, 583–597, doi:10.5194/tc-7-583-2013, 2013.

Fettweis, X.: Reconstruction of the 1979–2006 Greenland ice sheet surface mass balance using the regional climate model MAR, The Cryosphere, 1, 21–40, doi:10.5194/tc-1-21-2007, 2007.

Gunter, B., Urban, T., Riva, R., Helsen, M., Harpold, R., Poole, S., Nagel, P., Schutz, B., and Tapley, B.: A comparison of coincident GRACE and ICESat data over Antarctica, J. Geodesy, 83, 1051–1060, doi:10.1007/s00190-009-0323-4, 2009.

King, J. C.: The spatial coherence of interannual temperature variations in the Antarctic Peninsula, Geophys. Res. Lett., 30, 1040, doi:10.1029/2002GL015580, 2003.

King, J. C., Gadian, A., Kirchgaessner, A., Kuipers Munneke, P., Orr, A., Reijmer, C., Broeke, M. R., Van Wessem, J. M., and Weeks, M.: Validation of the summertime surface energy budgetof Larsen C Ice Shelf (Antarctica) as represented in three high-resolution atmospheric models, J. Geophys. Res.-Atmos., 120, 1335–1347, doi:10.1002/2014JD022604, 2015.

Kirchgäßner, A.: An analysis of precipitation data from the Antarctic base Faraday/Vernadsky, Int. J. Climatol., 31, 404–414, doi:10.1002/joc.2083, 2011.

Kuipers Munneke, P., Van den Broeke, M. R., Lenaerts, J. T. M., Flanner, M. G., Gardner, A. S., and Van de Berg, W. J.: A new albedo parameterization for use in climate models over the Antarctic ice sheet, J. Geophys. Res., 116, 1–10, doi:10.1029/2010JD015113, 2011.

Kuipers Munneke, P., Picard, G., van den Broeke, M. R., Lenaerts, J. T. M., and van Meijgaard, E.: Insignificant change in Antarctic snowmelt volume since 1979, Geophys. Res. Lett., 39, 6–10, doi:10.1029/2011GL050207, 2012.

Kuipers Munneke, P., Ligtenberg, S. R. M., Van Den Broeke, M. R., and Vaughan, D. G.: Firn air depletion as a precursor of Antarctic ice-shelf collapse, J. Glaciol., 60, 205–214, doi:10.3189/2014JoG13J183, 2014.

Kuipers Munneke, P., Ligtenberg, S. R., Suder, E. A., and Van Den Broeke, M. R.: A model study of the response of dry and wet firn to climate change, Ann. Glaciol., 56, 1–8, doi:10.3189/2015AoG70A994, 2015.

Lenaerts, J. T. M., Van den Broeke, M. R., Déry, S. J., Van Meijgaard, E., Van de Berg, W. J., Palm, S. P., and Sanz Rodrigo, J.: Modeling drifting snow in Antarctica with a regional climate model: 1. Methods and model evaluation, J. Geophys. Res., 117, 1–17, doi:10.1029/2011JD016145, 2012a.

Lenaerts, J. T. M., Van den Broeke, M. R., Van de Berg, W. J., Van Meijgaard, E., and Kuipers Munneke, P.: A new, high-resolution surface mass balance map of Antarctica (1979–2010) based on regional atmospheric climate modeling, Geophys. Res. Lett., 39, 1–5, doi:10.1029/2011GL050713, 2012b.

Lenaerts, J. T. M., Van den Broeke, M. R., Van Wessem, J. M., Van de Berg, W. J., Van Meijgaard, E., Van Ulft, L. H., and Schaefer, M.: Extreme precipitation and climate gradients in Patagonia revealed by high-resolution regional atmospheric climate modelling, J. Climate, 27, 4607–4621, doi:10.1175/JCLI-D-13-00579.1, 2014.

Ligtenberg, S. R. M., Helsen, M. M., and van den Broeke, M. R.: An improved semi-empirical model for the densification of Antarctic firn, The Cryosphere, 5, 809–819, doi:10.5194/tc-5-809-2011, 2011.

Ligtenberg, S. R. M., Kuipers Munneke, P., and van den Broeke, M. R.: Present and future variations in Antarctic firn air content, The Cryosphere, 8, 1711–1723, doi:10.5194/tc-8-1711-2014, 2014.

Luckman, A., Elvidge, A., Jansen, D., Kulessa, B., Kuipers Munneke, P., King, J., and Barrand, N. E.: Surface melt and ponding on Larsen C Ice Shelf and the impact of föhn winds,

Antarct. Sci., 26, 625–635, doi:10.1017/S0954102014000339, 2014.

Mouginot, J., Scheuchl, B., and Rignot, E.: Mapping of Ice Motion in Antarctica Using Synthetic-Aperture Radar Data, Remote Sens., 4, 2753–2767, doi:10.3390/rs4092753, 2012.

Peel, D. A.: Spatial temperature and accumulation rate variations at the Antarctic Peninsula, The Contributions of Antarctic Peninsula to Sea Level Rise, CEC Project Report EPOC-CT90-0015, 11–15, 1992.

Pritchard, H. D., Ligtenberg, S. R. M., Fricker, H. A., Vaughan, D. G., Van den Broeke, M. R., and Padman, L.: Antarctic ice-sheet loss driven by basal melting of ice shelves, Nature, 484, 502–5, doi:10.1038/nature10968, 2012.

Rignot, E., Velicogna, I., Van den Broeke, M. R., Monaghan, A., and Lenaerts, J. T. M.: Acceleration of the contribution of the Greenland and Antarctic ice sheets to sea level rise, Geophys. Res. Lett., 38, 1–5, doi:10.1029/2011GL046583, 2011.

Scambos, T. A., Hulbe, C., Fahnestock, M., and Bohlander, J.: The link between climate warming and break-up of ice shelves in the Antarctic Peninsula, J. Glaciol., 46, 516–530, doi:10.3189/172756500781833043, 2000.

Scambos, T. A., Berthier, E., Haran, T., Shuman, C. A., Cook, A. J., Ligtenberg, S. R. M., and Bohlander, J.: Detailed ice loss pattern in the northern Antarctic Peninsula: widespread decline driven by ice front retreats, The Cryosphere, 8, 2135–2145, doi:10.5194/tc-8-2135-2014, 2014.

Shepherd, A., Ivins, E. R., Geruo, A., Barletta, V. R., Bentley, M. J., Bettadpur, S., Briggs, K. H., Bromwich, D. H., Forsberg, R., Galin, N., Horwath, M., Jacobs, S., Joughin, I., King, M. A., Lenaerts, J. T. M., Li, J., Ligtenberg, S. R. M., Luckman, A., Luthcke, S. B., McMillan, M., Meister, R., Milne, G., Mouginot, J., Muir, A., Nicolas, J. P., Paden, J., Payne, A. J., Pritchard, H., Rignot, E., Rott, H., Sorensen, L. S., Scambos, T. A., Scheuchl, B., Schrama, E. J. O., Smith, B., Sundal, A. V., Van Angelen, J. H., Van de Berg, W. J., Van den Broeke, M. R., Vaughan, D. G., Velicogna, I., Wahr, J., Whitehouse, P. L., Wingham, D. J., Yi, D., Young, D., and Zwally, H. J.: A Reconciled Estimate of Ice-Sheet Mass Balance, Science, 338, 1183–1189, doi:10.1126/science.1228102, 2012.

Tapley, B. D., Bettadpur, S., Watkins, M., and Reigber, C.: The gravity recovery and climate experiment: Mission overview and early results, Geophys. Res. Lett., 31, 1–4, doi:10.1029/2004GL019920, 2004.

Thomas, E. R., Marshall, G. J., and McConnell, J. R.: A doubling in snow accumulation in the western Antarctic Peninsula since 1850, Geophys. Res. Lett., 35, 1–5, doi:10.1029/2007GL032529, 2008.

Thomas, E. R., Bracegirdle, T. J., Turner, J., and Wolff, E. W.: A 308 year record of climate variability in West Antarctica, Geophys. Res. Lett., 40, 5492–5496, doi:10.1002/2013GL057782, 2013.

Thompson, L., Peel, D., Mosley-Thompson, E., Mulvaney, R., Dal, J., Lin, P., Davis, M., and Raymond, C.: Climate since AD 1510 on Dyer Plateau, Antarctic Peninsula: evidence for recent climate change, Ann. Glaciol., 20, 420–426, doi:10.3189/172756494794587438, 1994.

Trusel, L. D., Frey, K. E., Das, S. B., Kuipers Munneke, P., and van den Broeke, M. R.: Satellite-based estimates of Antarctic surface meltwater fluxes, Geophys. Res. Lett., 40, 1–6, doi:10.1002/2013GL058138, 2013.

Turner, J., Colwell, S. R., and Harangozo, S.: Variability of precipitation over the coastal western Antarctic Peninsula from synoptic observations, J. Geophys. Res., 102, 13999, doi:10.1029/96JD03359, 1997.

Turner, J., Marshall, G. J., Morris, E. M., Mulvaney, R., and Winter, W.: Spatial variability of Antarctic Peninsula net surface mass balance, J. Geophys. Res., 107, 4–18, doi:10.1029/2001JD000755, 2002.

Turner, J., Colwell, S. R., Marshall, G. J., Lachlan-Cope, T. A., Carleton, A. M., Jones, P. D., Lagun, V., Reid, P. A., and Iagovkina, S.: Antarctic climate change during the last 50 years, Int. J. Climatol., 25, 279–294, doi:10.1002/joc.1130, 2005.

UCAR/NCAR/CISL/VETS: The NCAR Command Language (Version 6.2.1) [Software], doi:10.5065/D6WD3XH5, 2014.

Undén, P., Rontu, L., Jarvinen, H., Lynch, P., Calvo, J., Cats, G., Cuxart, J., Eerola, K., Fortelius, C., Garcia-moya, J., Jones, C., Lenderlink, G., Mcdonald, A., Mcgrath, R., and Navascues, B.: HIRLAM-5 Scientific Documentation, Tech. Rep. December, Swedish Meteorology and Hydrology Institute, 2002.

Van Angelen, J. H., Van den Broeke, M. R., Wouters, B., and Lenaerts, J. T. M.: Contemporary (1960–2012) Evolution of the Climate and Surface Mass Balance of the Greenland Ice Sheet, Surv. Geophys., 35, 1155–1174, doi:10.1007/s10712-013-9261-z, 2013.

Van Den Broeke, M. R.: The semi-annual oscillation and Antarctic climate. Part 2: recent changes, Antarct. Sci., 10, 175–183, doi:10.1017/S095410209800025X, 1998.

Van den Broeke, M. R.: Strong surface melting preceded collapse of Antarctic Peninsula ice shelf, Geophys. Res. Lett., 32, 2–5, doi:10.1029/2005GL023247, 2005.

Van Lipzig, N. P. M., King, J. C., and Lachlan-Cope, T. A.: Precipitation, sublimation, and snow drift in the Antarctic Peninsula region from a regional atmospheric model, J. Geophys. Res., 109, 1–16, doi:10.1029/2004JD004701, 2004.

Van Loon, H.: The Half-Yearly Oscillations in Middle and High Southern Latitudes and the Coreless Winter, J. Atmos. Sci., 24, 472–486, doi:10.1175/1520-0469(1967)024<0472:THYOIM>2.0.CO;2, 1967.

van Wessem, J. M., Reijmer, C. H., M. Lenaerts, J. T., van de Berg, W. J., van den Broeke, M. R., and van Meijgaard, E.: Updated cloud physics in a regional atmospheric climate model improves the modelled surface energy balance of Antarctica, The Cryosphere, 8, 125–135, doi:10.5194/tc-8-125-2014, 2014a.

Van Wessem, J. M., Reijmer, C. H., Morlighem, M., Mouginot, J., Rignot, E., Medley, B., Joughin, I., Wouters, B., Depoorter, M. A., Bamber, J. L., Lenaerts, J. T. M., Van De Berg, W. J., Van Den Broeke, M. R., and Van Meijgaard, E.: Improved representation of East Antarctic surface mass balance in a regional atmospheric climate model, J. Glaciol., 60, 761–770, doi:10.3189/2014JoG14J051, 2014b.

Van Wessem, J. M., Reijmer, C. H., Van de Berg, W. J., Van den Broeke, M. R., Cook, A. J., Van Ulft, L. H., and Van Meijgaard, E.: Temperature and Wind Climate of the Antarctic Peninsula as Simulated by a High-Resolution Regional Atmospheric Climate Model, J. Climate, 28, 7306–7326, doi:10.1175/JCLI-D-15-0060.1, 2015.

Vaughan, D. G., Marshall, G., Connolley, W. M., Parkinson, C., Mulvaney, R., Hodgson, D. A., King, J. C., Pudsey, C. J., and

Turner, J.: Recent Rapid Regional Climate Warming on the Antarctic Peninsula, Climatic Change, 60, 243–274, 2003.

Wouters, B., Martin-Español, A., Helm, V., Flament, T., van Wessem, J. M., Ligtenberg, S. R. M., van den Broeke, M. R., and Bamber, J. L.: Dynamic thinning of glaciers on the Southern Antarctic Peninsula, Science, 348, 899–903, doi:10.1126/science.aaa5727, 2015.

Wuite, J., Rott, H., Hetzenecker, M., Floricioiu, D., De Rydt, J., Gudmundsson, G. H., Nagler, T., and Kern, M.: Evolution of surface velocities and ice discharge of Larsen B outlet glaciers from 1995 to 2013, The Cryosphere, 9, 957–969, doi:10.5194/tc-9-957-2015, 2015.

Zwally, H. J., Giovinetto, M. B., Beckley, M. A., and Saba, J. L.: Antarctic and Greenland Drainage Systems, GSFC Cryospheric Sciences Laboratory, available at: http://icesat4.gsfc.nasa.gov/cryo_data/ant_grn_drainage_systems.php (last access: 29 January 2016), 2012.